



Photoluminescent properties of the europium and terbium complexes covalently bonded to functionalized mesoporous material PABA-MCM-41



José Arnaldo S. Costa^{a,*}, Roberta A. de Jesus^b, Diane D. Dorst^a, Ivo M. Pinatti^a,
Lucas M. da R. Oliveira^a, Maria E. de Mesquita^c, Caio Marcio Paranhos^a

^a Department of Chemistry, Federal University of São Carlos, 13565-905 São Carlos, São Paulo, Brazil

^b Institute of Chemistry and Biotechnology, Federal University of Alagoas, 57072-970 Maceió, Alagoas, Brazil

^c Department of Chemistry, Federal University of Sergipe, 49100-000 São Cristóvão, Sergipe, Brazil

ARTICLE INFO

Keywords:

Mesoporous material
Ln-PABA-MCM-41
Electron transitions
Photoluminescence properties

ABSTRACT

In this study, we describe the synthesis of the functionalized inorganic-organic material *p*-aminobenzoic acid MCM-41 by modification from *p*-aminobenzoic acid (PABA) and the covalently immobilization with rare earths (Eu^{3+} , Tb^{3+}) is also reported. The mechanism for the formation of the PABA-MCM-41 is known as the "Liquid Crystal Templating" (LCT) in which the liquid crystal molecules of a surfactant works as an organic template in the formation of the hexagonal structure. The complexes were characterized by FTIR, XRD, SAXS, N_2 adsorption/desorption, TGA, SEM, and luminescence analyses. The mesoporous materials exhibited the hexagonal mesostructures typical of the M41S family, as confirmed by XRD and SAXS, with high surface areas and thermal stability. The luminescent properties of the Tb-PABA-MCM-41 and Eu-PABA-MCM-41 complexes were more efficient, compared with pure $\text{Tb}(\text{PABA})_3$ and $\text{Eu}(\text{PABA})_3$ complexes, respectively. The more intense emissions are observed when the system is excited at the transition of the ligand. The lifetimes data of the Tb-PABA-MCM-41 complex presents longer lifetime (0.26 ms) than Eu-PABA-MCM-41 complex (0.12 ms).

1. Introduction

The M41S family of the mesoporous materials made up of silicate are considered promising for various applications such as support for catalysts [1,2], adsorbents [3–7], carriers of drug [8], sensors [9,10], optical devices [11], and others. The structure, composition and pore size of these materials may be formulated during the synthesis by varying of the reaction stoichiometry, the nature of the driver, the auxiliary chemicals, reaction conditions or by functionalization post-synthesis techniques [12]. The Mobil Composition of Matter No. 41 (MCM-41) has a hexagonal arrangement of uniformly sized pores and well defined [13] being extensively studied as molecular sieve due to its ease of synthesis (or synthesis facilities), thermal stability, high surface area (typically greater than $700 \text{ m}^2 \text{ g}^{-1}$) and acidity. Then the cylindrical structure with a high degree of symmetry found in pores of the MCM-41 made it a promising system for many applications.

The number of studies related to MCM-41 surface functionalization with organic groups has increased due to the variety of applications resulting in new chemical and versatile properties, since it is possible to adjust the surface of the mesoporous material (e.g., hydrophilicity, hydrophobicity, acidity, basicity, and mobilization) [11,14–16] and

then, with the reactivity surface altered the protection from others chemical attacks is ensured [12].

Within this context, in the last years many studies have focused on the functionalization of the MCM-41 with luminescent metallic complexes of the europium and terbium [11,14,15,17–21]. It is reported that its photoluminescent properties could be modified by the interaction of a host structure, since the low photoluminescent of these rare earth complexes limit their practical applications [11]. Previous studies have reported the luminescent properties of the europium and/or terbium complexes anchored in the different ligands and materials. Fernandes et al. [17], Gu and Yan [15], Li and Yan [21], Zang et al. [22], Yu et al. [23], Wang et al. [24], Meng et al. [25], and Liu et al. [26] have obtained the $\text{Eu}(\text{thd})_x/\text{MCM-41}$, $\text{EuL}_3\text{phen-MCM-41}$, Ln-MMBA-MCM-41, $\text{Eu}(\text{DBM})_3\text{Phen/PMMA}$, $\text{Eu}_2\text{O}_3\text{-ZnO/(SBA-15)}$, $\text{Ln}(\text{bpy})_n\text{-zeolite L}$, $\text{Eu}(\text{DBM})_{3.2}\text{H}_2\text{O MCM-48}$, and $(\text{Ln})\text{SSA/(SBA-15)}$ hybrid materials, respectively.

Historically, lanthanide ion-containing complexes are well known for their intense emission lines on ultraviolet light irradiation. This property is a consequence of the effective intramolecular energy transfer process of the ligands coordinated to the luminescent central lanthanide ion, which in turn undergoes the corresponding radiative

* Corresponding author.

E-mail address: josearnaldo23@yahoo.com.br (J.A.S. Costa).

emission process (known as "antenna effect") [27]. The radiation incident on the material can be absorbed by the organic ligand that acts as "antenna", which is transferred from the excited state of the ligand to the metal ion which then emits its characteristic radiation in the electromagnetic spectrum range [28–30]. Thus, complexes of trivalent lanthanide ions have interesting and specific properties for various optical applications [28] as the use of Eu^{3+} and Tb^{3+} as the light conversion devices, such as waste markers gunpowder and the use of Eu^{3+} as a structural probe for the investigation of forming around the ion emitter [28].

In the present study, the hybrid luminescent lanthanide complexes were obtained by introduction of Ln^{3+} (Eu^{3+} and Tb^{3+}) into the functionalized MCM-41 with para-aminobenzoic acid modifier (PABA-MCM-41).

2. Materials and methods

2.1. Standards, solvents, and reagents

The europium (III) and terbium (III) chloride (Aldrich), cetyltrimethylammonium bromide (CTAB, Vetec), ethanol (Tedia), chloroform (Tedia), tetraethylorthosilicate (TEOS, Aldrich), *p*-aminobenzoic acid (PABA, Aldrich), and ammonia monohydrate ($\text{NH}_3 \cdot \text{H}_2\text{O}$, Synth) were all used without further purification. Ultrapure water was obtained from a Milli-Q system (Millipore Co.).

2.2. Synthetic procedure

2.2.1. Synthesis of mesoporous MCM-41 material functionalized with PABA (PABA-MCM-41)

The synthesis of PABA-MCM-41 was performed according to the methodology described previously [4], with the final molar composition: 0.12 CTAB:0.50 $\text{NH}_3 \cdot \text{H}_2\text{O}$:0.96 TEOS:0.04 PABA-Si:58.24 H_2O . The CTAB surfactant was removed from the synthesized materials by refluxing in a solution of 1.0 mol L^{-1} $\text{CH}_3\text{CH}_2\text{OH}/\text{HCl}$ for 48 h [4,5]. The final solid products were filtered, washed with deionized water, and dried under vacuum at ambient temperature.

2.2.2. Synthesis of PABA-MCM-41 mesoporous material covalently bonded with the lanthanide (Ln^{3+}) complexes (Ln-PABA-MCM-41, Ln = Tb, Eu)

The hybrid mesoporous material was prepared followed the procedure described by [16], with modifications: PABA-MCM-41 was immersed in an appropriate LnCl_3 ethanol solution volume with 1:3 (Ln^{3+} :PABA-Si) molar ratio. The mixture was heated under reflux for 24 h, under a nitrogen atmosphere, filtrated, and extensively washed with ethanol. The Ln-PABA-MCM-41 obtained was dried under vacuum overnight.

2.3. Characterization of the mesoporous materials

The Fourier transform infrared spectroscopy (FTIR) spectra were obtained in the region 4000–400 cm^{-1} using a Varian 3100 spectrophotometer, operated at ambient temperature, with a resolution of 4 cm^{-1} , and number of scans equal to 32. The samples were prepared in the form of KBr pastilles.

The crystallographic identification of the mesoporous materials were obtained on a Siemens (model D-5000) diffractometer equipped with a $\text{Cu K}\alpha$ ($\lambda = 1.5406 \text{ \AA}$) radiation source. The X-ray diffractometry (XRD) patterns were obtained at room temperature, in the 2θ range of 1–10°, in step scan mode with a width of 0.02°, a step time of 6 s, and with a scan rate of 0.2° min^{-1} .

The small-angle X-ray scattering (SAXS) experiments were performed in a Bruker AXS 2D Nanostar (EUA) with $\text{CuK}\alpha$ radiation, operating at 40 kV/35 mA in a range of 0.01–3.60 \AA^{-1} . The sample-to-detector distance was fixed at 107 cm, and the time-resolved spectra of

the nanocomposites were collected every 1200 s, with a minimum resolution in $q = 0.00628 \text{ \AA}^{-1}$.

Nitrogen adsorption–desorption isotherms were obtained at $-196.15 \text{ }^\circ\text{C}$ using a NOVA 1200 volumetric adsorption analyzer. Prior to the analysis, approximately 100 mg of sample was evacuated at 150 $^\circ\text{C}$ for 1 h in the degas port of the instrument. The Brunauer-Emmett-Teller (BET) specific surface area was calculated using adsorption data in the relative pressure range from 0.01 to 0.95. The pore volume of the samples were determined from the amount of nitrogen adsorbed at a relative pressure of about 0.95, and pore size distribution curves were calculated from analysis of the adsorption branch of the isotherm using the Barrett-Joyner-Halenda (BJH) algorithm.

Thermogravimetric analyses (TGA) were performed under a 40 mL min^{-1} flow of nitrogen using a Shimadzu TGA-50 balance. Portions of samples (~ 5.0 mg) were placed in platinum crucibles and the temperature was increased from 35 to 900 $^\circ\text{C}$ at a heating rate of 10 $^\circ\text{C min}^{-1}$.

Scanning electron microscopy (SEM) images were obtained at a magnification of 200–10,000 using a Leica-Zeiss LEO 440 microscope operated at an acceleration voltage of 15–25 kV, with a secondary electron detector positioned approximately 13–25 mm from the sample.

The luminescence study was based on the excitation and emission spectra recorded at room temperature (300 K). The data was obtained in a 1940D Spectrofluorometer (HORIBA, Jobin Yvon-Fluorolog III) with double monochromators in front face mode (22.5°) with a USHIO™ UXL-450SO 450 W xenon gas discharge lamp as excitation source. Luminescence decay curves were recorded in a SPEX1934D phosphorimeter accessory with a EXCELITAS™ FX-1102 Short Arc Xenon Flash lamp, 0.15 J per flash, 10 W Average Power and 300 Hz Flash Rate.

3. Results and discussion

3.1. Characterization of the mesoporous materials

3.1.1. Fourier transform infrared spectroscopy (FTIR)

The FTIR spectra for the PABA, $\text{Eu}(\text{PABA})_3$, $\text{Tb}(\text{PABA})_3$, PABA-MCM-41, Eu-PABA-MCM-41 , and Tb-PABA-MCM-41 compounds are shown in Fig. 1. Narrow bands centered at around 3460–3360 cm^{-1} corresponded to stretching of the N–H bond of the primary amine on the PABA, and at 1290 cm^{-1} (C–N stretching) is characteristic of the amine group bonded to the aromatic ring of the PABA (Fig. 1a). The bands centered at around 3229–2804 (O–H stretching) and at 1668 cm^{-1} (C = O stretching) are characteristic of the carboxylic acid functional group [31]. The coordination of the lanthanide ions to the PABA, for the formation of the $\text{Eu}(\text{PABA})_3$ and $\text{Tb}(\text{PABA})_3$ complexes, was evidenced by the intensity reduction of the bands related to the carboxylic acid functional group (Fig. 1b and c).

The presence of the organic PABA bonded in the mesoporous silica MCM-41 was confirmed by FTIR. The spectrum of the PABA-MCM-41 (Fig. 1d), shows absorption bands in ν (stretch C–Si, 1199 cm^{-1}), ν (stretch Si–O, 1086 cm^{-1}) which is characterized by the trialkoxysilane function. The presence of the band at 1647 cm^{-1} corresponds to an absorption of the amide group, and the bands centered at 2928 and 2849 cm^{-1} correspond to methylene ($-(\text{CH}_2)_3-$) of the TEPIC on PABA grafted which proves the covalent bond formation [4,16]. In addition, a band at 1553 cm^{-1} confirms an amide functional group formation.

The broad and intense absorption band in the region between 3182 and 3719 cm^{-1} corresponds to the stretches of the O–H bond the water molecules adsorbed on the mesoporous materials and the presence of the silane groups (Si–OH). Analyzing the absorption spectra of the PABA-MCM-41, Eu-PABA-MCM-41 , and Tb-PABA-MCM-41 (Fig. 1d, e, and f, respectively), it is possible to observe the characteristic formation of the condensed silica (Si–O–Si), by the bands at 1086 and 804 cm^{-1} for the Si–O bond and the 460 cm^{-1} band for the Si–O–Si binding [5,7,16,32]. In addition, as corresponding bands of the PABA anchored

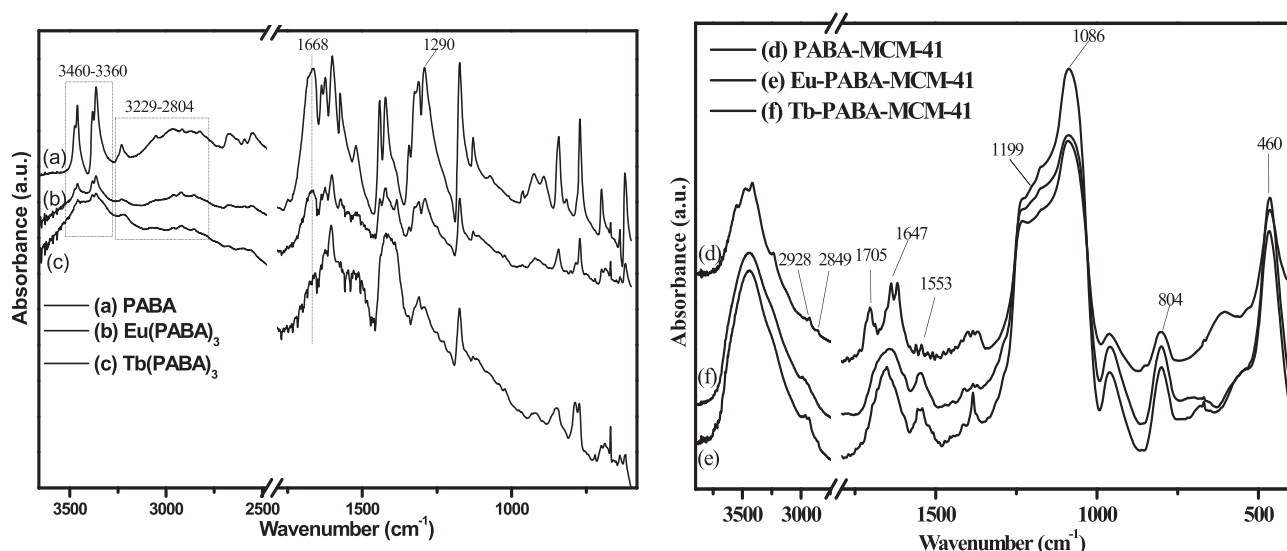


Fig. 1. FTIR spectra of (a) PABA, (b) Eu(PABA)₃, (c) Tb(PABA)₃, (d) PABA-MCM-41, (e) Eu-PABA-MCM-41, and (f) Tb-PABA-MCM-41 materials.

in the MCM-41, were observed in the lower region of energy, such as $\nu(-\text{CONH}-)$ 1647 and 1553 cm^{-1} , $\nu(-(\text{CH}_2)_3-)$ 2928 and 2849 cm^{-1} and the band at 1705 cm^{-1} related to the asymmetric stretch $\text{C}=\text{O}$ of the carboxylic acid in the Eu-PABA-MCM-41 and Tb-PABA-MCM-41 mesoporous materials. This is an indication of the coordination of the lanthanide ions to the group PABA in silica supports [33].

The coordination of the metal ions occurs by the group COO^- , the band attributed to this group is shifted in the Eu-PABA-MCM-41 and Tb-PABA-MCM-41 spectra of 50 and 66 cm^{-1} , respectively. Based on these data, a higher degree of covalence can be observed in the Tb-PABA-MCM-41 and this is probably related to the greater shifting of the band corresponding to carbonyl which favors the energy transfer process from PABA to the lanthanide ions. In addition, the displacement of the band to the lower energy region may be indicative of the increase in the length of the bonds that surround the oxygen atom [34,35]. The low intensity band around ν 470 cm^{-1} characteristic of the Eu-O and Tb-O bond are overlapping the silica bands at ν 460 cm^{-1} .

3.1.2. X-ray diffractometry (XRD) and small-angle X-ray scattering (SAXS) characterizations

X-ray measurements, especially XRD and SAXS, are popular and efficient methods for characterizing highly ordered mesoporous materials with hexagonal symmetry of the $p6mm$ space group. The XRD and SAXS profiles for PABA-MCM-41, Eu-PABA-MCM-41, and Tb-PABA-MCM-41 are shown in Figs. 2 and 3, respectively. According to Fig. 2, the pattern for all materials clearly shows the order of the hexagonal matrix of the synthesized materials which is typical of the M41S family, with the distinct Bragg diffraction peaks in the range of $2-10^\circ$, which can be indexed as reflections of Miller (1 0 0), (1 1 0), and (2 0 0) which are related to the peaks q_{100} and q_{110} as shown in Fig. 3 [4,7,11,36]. However, the Eu-PABA-MCM-41 and Tb-PABA-MCM-41 reflection planes (1 0 0), (1 1 0), and (2 0 0) were observed at larger angles than the PABA-MCM-41. The planes (1 1 0) and (2 0 0) for the both lanthanide functionalized materials (Eu and Tb) presented lower intensity when compared to the PABA-MCM-41 matrix. This is related to the scattering difficulty of the X-rays in the pores of the mesoporous materials after the lanthanides incorporation resulting in a reduction of the mesoporous ordering, but not in the collapse of the pores structure of the mesoporous materials.

The position of the first peak, d_{100} , allows determining the direction of the central distance between adjacent tubes, using [7]:

$$a_0 = \left(\frac{2}{\sqrt{3}}\right) d_{100} \quad (1)$$

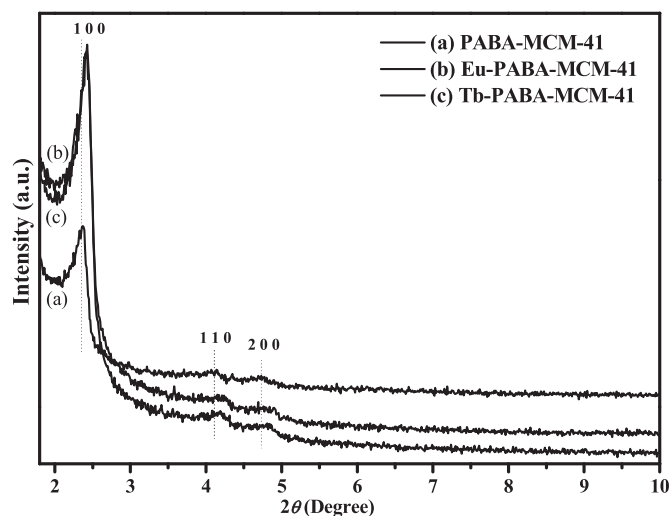


Fig. 2. XRD profile of (a) PABA-MCM-41, (b) Eu-PABA-MCM-41, and (c) Tb-PABA-MCM-41 mesoporous materials.

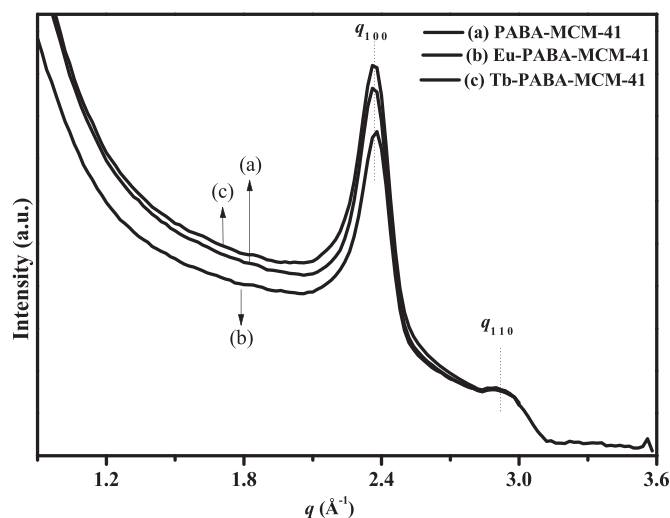


Fig. 3. X-ray scattering intensity of (a) PABA-MCM-41, (b) Eu-PABA-MCM-41, and (c) Tb-PABA-MCM-41 mesoporous materials.

Table 1
Textural and structural properties of the mesoporous materials.

Mesoporous material	S_{BET} ($m^2 g^{-1}$)	d_{100} (nm)	V ($cm^3 g^{-1}$)	D_{BJH} (nm)	a_0 (nm)
MCM-41 [5]	617	4.06	0.39	3.92	4.69
PABA-MCM-41	556	3.74	0.35	3.61	4.31
Eu-PABA-MCM-41	396	3.66	0.26	1.69	4.22
Tb-PABA-MCM-41	361	3.63	0.24	1.68	4.19

d_{100} : $d(100)$ spacing; a_0 : center-center distance ($a_0 = (2/\sqrt{3})d$); S_{BET} : BET surface area; V : pore volume, and D_{BJH} : pore diameter.

where d_{100} is given by

$$d_{100} = \frac{\lambda}{2 \sin \theta} \quad (2)$$

The calculated values of d and a_0 for PABA-MCM-41, Eu-PABA-MCM-41, and Tb-PABA-MCM-41 are provided in Table 1. The decrease in the values of the S_{BET} , d_{100} , V , D_{BJH} , and a_0 for the MCM-41 was attributed to the immobilization of the PABA ligand and lanthanide ions into the pores of the mesoporous material. The pore diameters reflect a reducing trend in the pore size, from 3.92 nm (MCM-41) to 3.61 nm (PABA-MCM-41), due to the presence of PABA organic ligand into the pores of pure MCM-41. As well as a reduction from 3.61 nm in the PABA-MCM-41 to ~ 1.68 nm in the Ln-PABA-MCM-41 complexes, due to the coordination of the lanthanide ions to the group PABA into the mesoporous support. Thus, it is possible suggest that the size of the Ln (PABA)₃ complex covalently bounded into the pores of MCM-41 is approximately 2.28 nm.

3.1.3. Thermogravimetric analyses (TGA)

Fig. 4a and b show the TGA/DTGA curves obtained for the PABA-MCM-41, Eu-PABA-MCM-41, and Tb-PABA-MCM-41 synthesized materials. It is possible to observe that the PABA-MCM-41 presented a mass loss event at temperature range between 30 and 185 °C, which could be attributed to the elimination of physically adsorbed water in the silica and to the residual solvents. Two more mass loss events are observed in this material. The first one is observed at temperature range between 185 and 380 °C corresponding to 6.22% of mass loss, which is related to a partial decomposition of the organic matter of PABA anchored in the MCM-41, and the second loss between 380 and 750 °C corresponding to 1.5% of mass loss, which is attributed to the combustion of the PABA residual organic matter, as well as condensation of adjacent silanol groups resulting from linking of the siloxanes situated

within the pores of Si-MCM-41 [4,7,32,37–40]. Thus, it can be inferred that the mass percentage of the PABA functionalizing group, bonded in the MCM-41 silica, corresponds to approximately the total mass loss in the last two events, around 7.72%.

The thermogravimetric curves for Eu-PABA-MCM-41 and Tb-PABA-MCM-41 were typical of mesoporous materials based on MCM-41. There were three main processes of mass loss to both materials. The first loss of water physically adsorbed and the residual solvents comprised in the temperature range of 30–170 °C (6% mass loss) and 30–140 °C (4,5% mass loss) for Eu-PABA-MCM-41 and Tb-PABA-MCM-41, respectively. The second weight loss event is related to the decomposition of PABA organic part of MCM-41 mesoporous at 170–330 °C and 170–340 °C temperature range for Eu-PABA-MCM-41 and Tb-PABA-MCM-41, respectively. Finally, the last mass loss event refers to the decomposition of the europium and terbium chlorides in the temperature range between 500–700 °C and 400–745 °C in the materials.

3.1.4. Scanning electron microscopy (SEM)

The SEM images obtained for the PABA-MCM-41, Eu-PABA-MCM-41, and Tb-PABA-MCM-41 mesoporous materials are shown in Fig. 5. The SEM images were used to determine the morphology of the synthesized mesoparticles. The mesoporous materials presented the agglomerated spherical particles that are a typical feature of the M41S family, with high homogeneity [4]. This homogeneity was observed because of strong covalent bonds bridging between the inorganic and organic phases of the complexes (Eu-PABA-MCM-41 and Tb-PABA-MCM-41) [16].

3.1.5. Photoluminescence properties

Luminescence measurements were performed on Tb-PABA-MCM-41, Eu-PABA-MCM-41 mesoporous materials and their respective Tb (PABA)₃ and Eu(PABA)₃ complexes at room temperature. The excitation and emission spectra of the Tb-PABA-MCM-41 and Tb(PABA)₃ complexes are shown in Figs. 6 and 7, respectively. The excitation spectrum of Tb-PABA-MCM-41 monitoring the emission at 547 nm (⁵D₄ → ⁷F₅) shows a large broad band between 250 and 370 nm which is attributed to light absorption by modification with PABA. Comparing with the Tb(PABA)₃ complex, the excitation band is narrower and the maximum excitation wavelength of 337 nm in Tb-PABA-MCM-41 shifts to 303 nm in Tb(PABA)₃. This behavior in Tb-PABA-MCM-41 is due to the hypsochromic effect resulting from the change in the polarity of the environment around the Tb(PABA)₃ in the mesoporous material [41]. Fig. 7 presents emission spectra of the Tb(PABA)₃ and Tb-PABA-MCM-41 complexes excited at 303 and 337 nm, respectively. Analyzing the

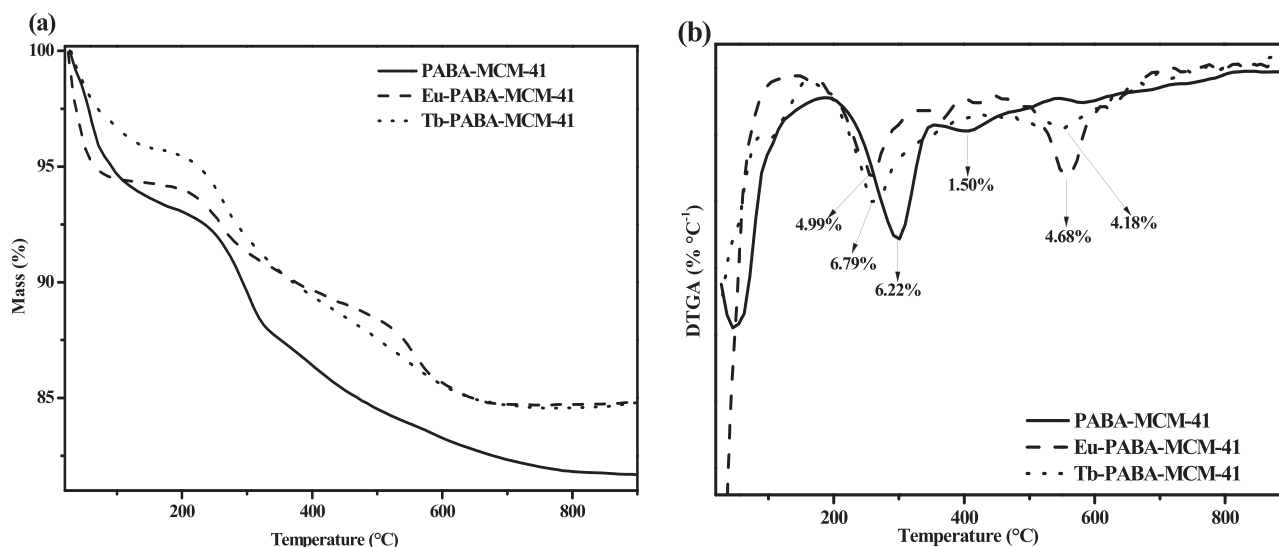


Fig. 4. (a) TGA and (b) DTGA curves for PABA-MCM-41, Eu-PABA-MCM-41, and Tb-PABA-MCM-41 mesoporous materials.

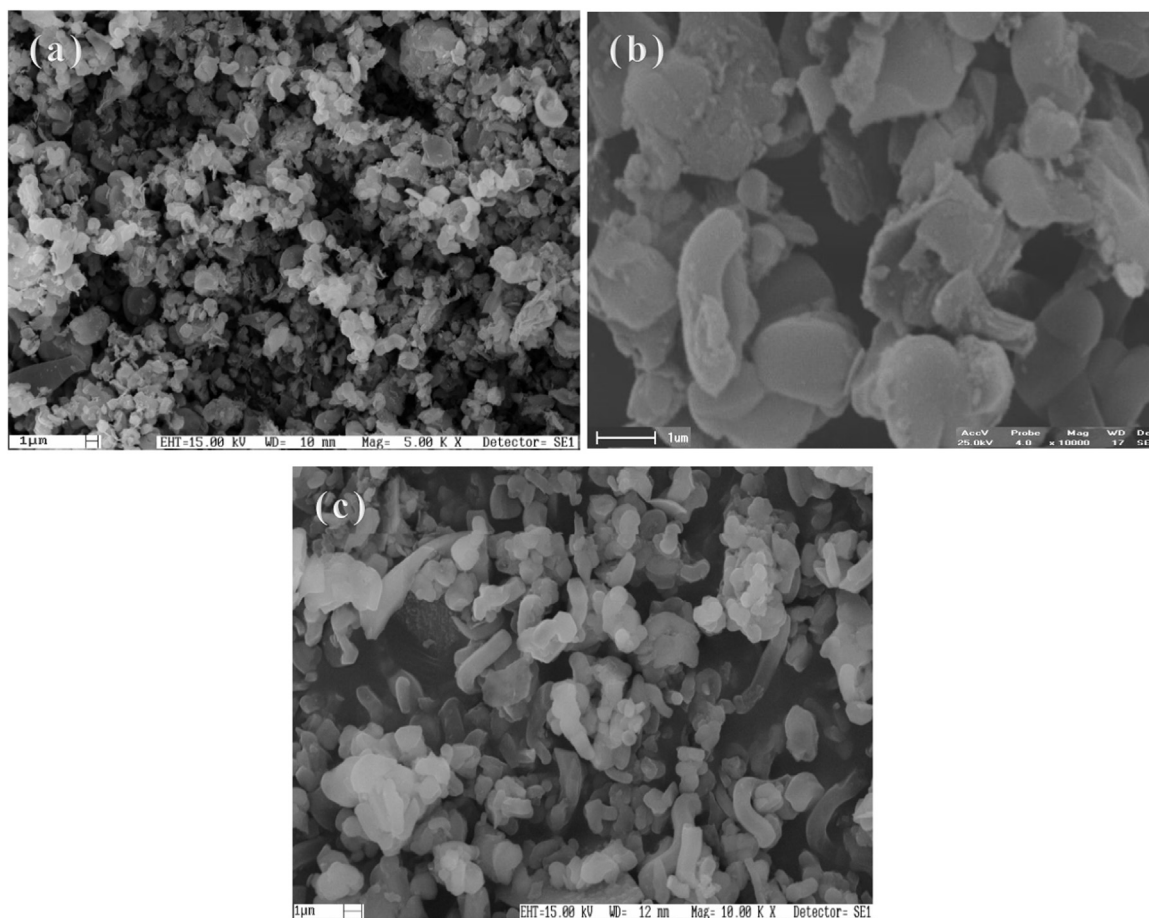


Fig. 5. Scanning electron micrograph of (a) PABA-MCM-41 [4], (b) Eu-PABA-MCM-41, and (c) Tb-PABA-MCM-41.

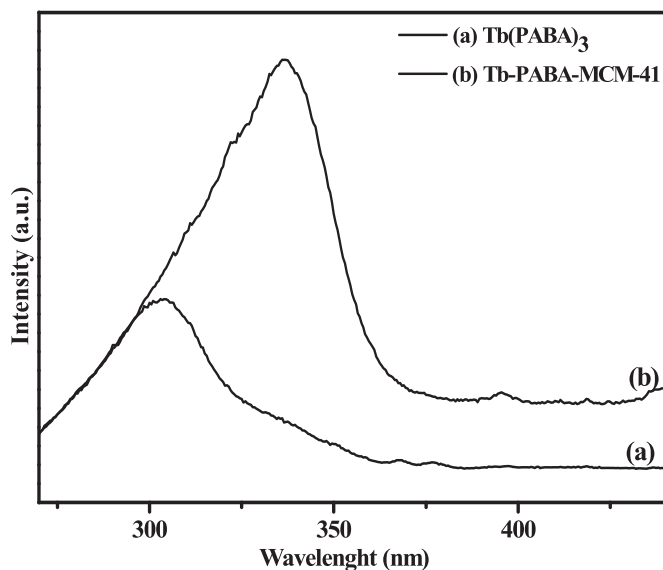


Fig. 6. Excitation spectra of (a) $Tb(PABA)_3$ and (b) $Tb-PABA-MCM-41$ complexes.

emission spectra of the $Tb(PABA)_3$ and $Tb-PABA-MCM-41$, four bands are clearly observed in the range of 400–750 nm, which are assigned to $^5D_4 \rightarrow ^7F_J$ ($J = 6-3$) transitions at 488, 548, 588, and 624 nm, respectively in both spectra. These results indicate that occurred effective energy transfer between the modified PABA and the chelated Tb^{3+} ions. The $Tb-PABA-MCM-41$ hybrid mesoporous material exhibits emissions by virtue of the chemically covalent molecular bond of the

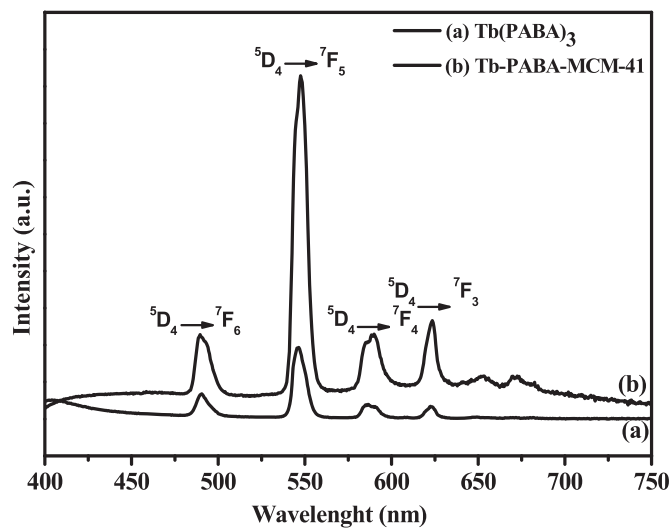


Fig. 7. Emission spectra of (a) $Tb(PABA)_3$ and (b) $Tb-PABA-MCM-41$ complexes.

Si–O network structure between the complex and the mesoporous silica.

The excitation and emission spectra of the $Eu-PABA-MCM-41$ and $Eu(PABA)_3$ complexes are shown in Figs. 8 and 9, respectively. The excitation spectrum was obtained monitoring the $^5D_0 \rightarrow ^7F_2$ transition of Eu^{3+} at 616 nm. By analyzing the spectrum it is possible to observe a broad band in the range between 275 and 390 nm due to $Eu-O$ charge transfer processes and electron transitions of PABA. The excitation spectrum also contains strong and narrow peaks originating from Eu^{3+} f–f transitions in the range 360–450 nm which can be assigned to the

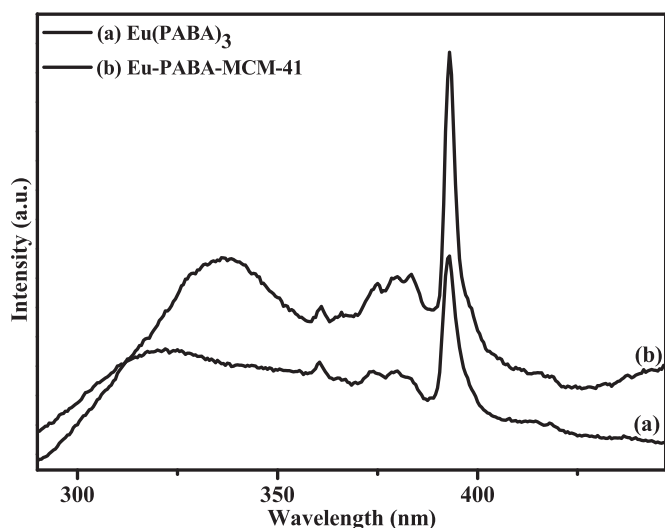


Fig. 8. Excitation spectra of (a) Eu(PABA)₃ and (b) Eu-PABA-MCM-41 complexes.

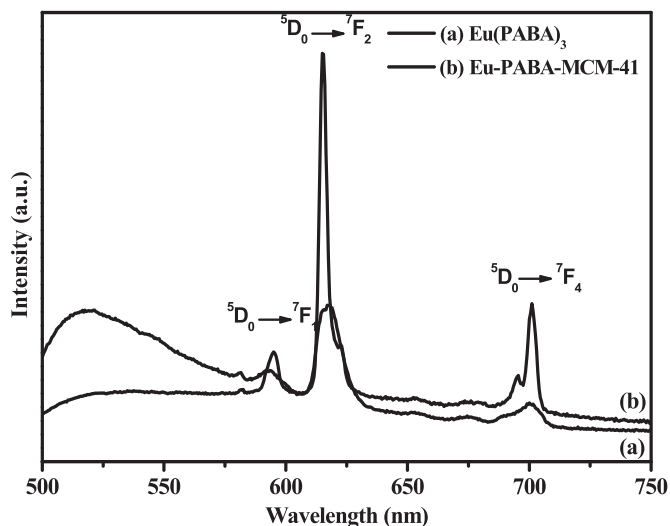


Fig. 9. Emission spectra of (a) Eu(PABA)₃ and (b) Eu-PABA-MCM-41 complexes.

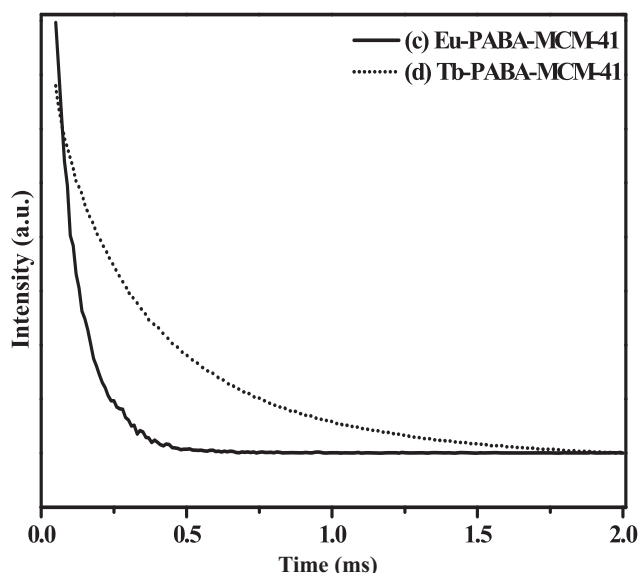
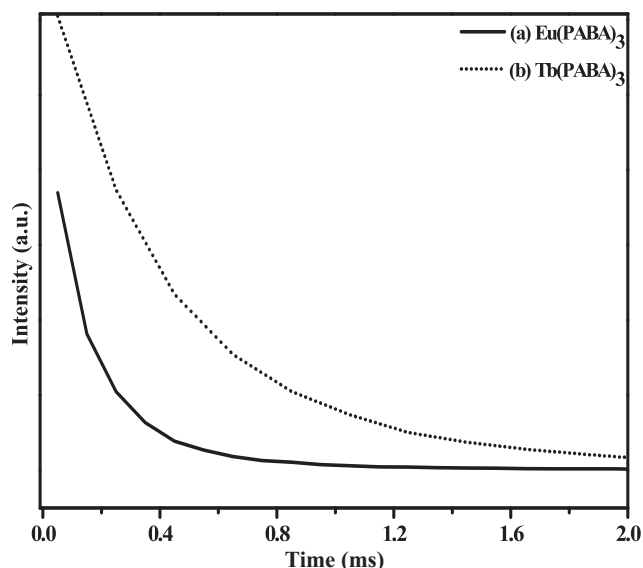


Fig. 10. The luminescence decay curves of (a) Eu(PABA)₃, (b) Tb(PABA)₃, (c) Eu-PABA-MCM-41, and (d) Tb-PABA-MCM-41 complexes.

${}^7F_0 \rightarrow {}^5D_4$ (362 nm), ${}^7F_0 \rightarrow {}^5L_{7,8}$ (384 nm), and ${}^7F_0 \rightarrow {}^5L_6$ (394 nm) transitions. Analyzing the emission spectra of the Eu(PABA)₃ and Eu-PABA-MCM-41 three bands are observed in the range 500–750 nm, which are assigned ${}^5D_0 \rightarrow {}^7F_1$, ${}^5D_0 \rightarrow {}^7F_2$, and ${}^5D_0 \rightarrow {}^7F_4$ transitions at 595, 615, and 703 nm, respectively. The electric dipole transition ${}^5D_0 \rightarrow {}^7F_2$ is sensitive to local symmetry while the ${}^5D_0 \rightarrow {}^7F_1$ is little affected by the environment. Once, the ${}^5D_0 \rightarrow {}^7F_2$ transition evidence a stronger emission, it indicates that Eu³⁺ occupies a site that lacks inversion symmetry [42,43].

3.1.6. Luminescence decay times (s), emission quantum efficiency (η), and Judd-Ofelt intensity parameters (Ω_λ)

Fig. 10 shows the photoluminescence decay curves of Eu(PABA)₃, Tb(PABA)₃, Eu-PABA-MCM-41, and Tb-PABA-MCM-41 complexes. They were measured at room temperature and both curves could be well fitted in a first order exponential function represented in Eq. (3):

$$I(t) = I_0 e^{-\frac{t}{\tau}} \quad (3)$$

where $I(t)$ is intensity at a given time t , I_0 is initial intensity, and τ is a decay constant (lifetime).

The single behavior of the decay curves implies only one depopulation mechanism of the excited levels, which attests for the occurrence of a single coordination site for the Eu³⁺ and Tb³⁺ ions, yielding lifetimes of 0.27, 0.13, 0.26, and 0.12 ms for Tb(PABA)₃, Eu(PABA)₃, Tb-PABA-MCM-41, and Eu-PABA-MCM-41 complexes, respectively (Table 2). The τ values obtained for the europium complexes were coherent with those found for the SiO₂-PMMA hybrid (S0) [44], Eu (DDBM)₃H₂O and Eu₂(DDBM)₃H₂O complexes [45], and Lu₂O₃:Eu³⁺ nanocrystals [46], as well as the τ values obtained for the terbium complexes were similar to reported by Mani et al. [47], Massey et al. [48], and Kottas et al. [49].

The emission quantum efficiency (η) of the 5D_0 emitting level from Eu³⁺ ion is given by the following equation [3,50]:

$$\eta = \frac{A_{rad}}{A_{total}} \quad (4)$$

The total decay rate of spontaneous emission is:

$$A_{total} = (1/\tau) = A_{rad} + A_{nrad} \quad (5)$$

where A_{rad} is given by:

$$A_{rad} = \sum_J A_{0 \rightarrow J} \quad (6)$$

Table 2
Photoluminescent data of the complexes.

Complexes	τ (ms)	τ^{-1} (10^3 s^{-1})	A_{rad} (10^3 s^{-1})	A_{nrad} (10^3 s^{-1})	η (%)	Ω_2 (10^{-20} cm^2)	Ω_4 (10^{-20} cm^2)
Tb(PABA) ₃	0.27	3.703	–	–	–	–	–
Eu(PABA) ₃	0.13	7.692	0.148	7.544	1.92	2.66	1.16
Tb-PABA-MCM-41	0.26	3.846	–	–	–	–	–
Eu-PABA-MCM-41	0.12	8.333	0.227	8.106	2.73	3.90	3.14

thus, A_{rad} and A_{nrad} are the radiative and non-radiative rates, respectively. The coefficients $A_{0 \rightarrow J}$ are determined assuming the ${}^5\text{D}_0 \rightarrow {}^7\text{F}_1$ transition governed by the magnetic dipole as an internal standard because the $A_{0 \rightarrow 1}$ rate is almost insensitive to changes in the chemical environment around the europium ion. The spontaneous emission A_{01} is found in the emission spectra and can be estimated according to equation below, where σ_1 is the respective barycentre energy and n is the refractive index [50,51].

$$A_{01} = 0.31 \times 10^{-11} n(\sigma_1)^3. \quad (7)$$

It was assumed that n would be equal to 1.5. Other spontaneous emission coefficients A_{0J} ($J = 0, 2, 3,$ and 4) were obtained by the following equation [3,50,51].

$$A_{0 \rightarrow J} = A_{0 \rightarrow 1} \frac{\sigma_{0 \rightarrow 1} S_{0 \rightarrow J}}{\sigma_{0 \rightarrow J} S_{0 \rightarrow 1}}, \quad (8)$$

where S_{01} and S_{0J} are the integrated intensities of the ${}^5\text{D}_0 \rightarrow {}^7\text{F}_1$ and ${}^5\text{D}_0 \rightarrow {}^7\text{F}_J$ ($J = 0, 2, 3,$ and 4) transitions, and σ_{01} and σ_{0J} are their barycentre energies, respectively. Finally, the Judd-Ofeld intensity parameters Ω_λ ($\lambda = 2, 4$ or 6) were calculated from Jesus et al. [44]:

$$\Omega_\lambda = \frac{3\hbar \cdot A_{0 \rightarrow J}}{64\pi^4 \cdot e^2 \cdot \bar{\nu}_{0 \rightarrow J}^3 \cdot \chi \cdot \langle {}^7\text{F}_J | U^{(\lambda)} | {}^5\text{D}_0 \rangle^2} \quad (9)$$

where \hbar is the Planck constant under 2π , $A_{0 \rightarrow J}$ is the Einstein coefficient related to ${}^5\text{D}_0 \rightarrow {}^7\text{F}_J$ transition, e is the elementary charge, $\bar{\nu}_{0 \rightarrow J}$ is the barycenter of the transition, χ is the Lorentz factor, and $\langle {}^7\text{F}_J | U^{(\lambda)} | {}^5\text{D}_0 \rangle^2$ is a matrix element [44].

The experimental values of radiative and non-radiative rates of the spontaneous emission (A_{rad} and A_{nrad} , respectively), quantum efficiency (η), and Judd-Ofeld intensity parameters (Ω_λ) for Eu(PABA)₃ and Eu-PABA-MCM-41 complexes are summarized in Table 2. The quantum efficiency (η) of the Eu-PABA-MCM-41 is low due to the higher A_{nrad} (8106 s^{-1}) compared to A_{rad} (227 s^{-1}). This may be predominantly a result of large number of non-radiative channels in the material which contribute to the low efficiency of electron transfer, at which the values of η were 1.92 and 2.73% for Eu(PABA)₃ and Eu-PABA-MCM-41 complexes, respectively. However, the difference between this values is explained by a higher A_{rad} value found for the Eu-PABA-MCM-41 complex, compared to the Eu(PABA)₃ complex [52]. The low values obtained for η in the complexes were similar to reported by Li and Yan [16], Jesus et al. [44], and Kolesnikov et al. [46]. Finally, comparing the Eu-PABA-MCM-41 and Eu(PABA)₃ complexes, in both cases $\Omega_2 > \Omega_4$, indicating that Eu^{3+} ions are localized in a more symmetric environment. Also, the Eu-PABA-MCM-41 mesoporous material presents higher values of Ω_2 and Ω_4 compared to the Eu(PABA)₃ complex. These results suggest that Eu^{3+} environment changes from high symmetry to low symmetry [44]. The Ω_2 value obtained for the Eu-PABA-MCM-41 was higher than the values reported by Beltaif et al. [53], Ferhi et al. [54], Hassairi et al. [55], Koubaa et al. [56], and Ramakrishna et al. [57]. As well as the Ω_4 value was higher than the values reported by Jesus et al. [44], Beltaif et al. [53], Carlos et al. [58], Liang and Xie [59], Luo et al. [45], and Ramakrishna et al. [57].

4. Conclusions

In the present study, a hydrothermal/co-condensation method was

successfully used to synthesize a mesoporous material functionalized with the *p*-aminobenzoic acid ligand modified with 3-(triethoxysilyl)propyl isocyanate, posteriorly the lanthanide (Eu^{3+} , Tb^{3+}) complexes have been successfully covalently immobilized in the PABA-MCM-41. The synthesized PABA-MCM-41, Eu-PABA-MCM-41, and Tb-PABA-MCM-41 mesoporous materials exhibited the hexagonal mesostructures typical of the M41S family, as confirmed by XRD and SAXS, with high surface areas and thermal stability. The hybrid mesoporous materials exhibits emissions by virtue of the chemically covalent molecular bond of the Si–O network structure between the complexes and the ordered mesoporous silica. The luminescent properties of mesoporous materials Tb-PABA-MCM-41 and Eu-PABA-MCM-41 were more efficient, compared with pure Tb(PABA)₃ and Eu(PABA)₃ complexes, respectively, with more intense emissions when the system is excited at the transition of the ligand. The lifetimes data of the mesoporous material Tb-PABA-MCM-41 presents a longer lifetimes (0.26 ms) than Eu-PABA-MCM-41 (0.12 ms).

Acknowledgments

The authors thank CNPq (Conselho Nacional de Desenvolvimento Científico e Tecnológico) (Processes 309342/2010-4 and 135602/2011-4), CAPES (Coordenação de Aperfeiçoamento de Pessoal de Nível Superior) (Process 309342/2010-4), and FAPESP (Fundação de Amparo à Pesquisa do Estado de São Paulo) (Processes 2013/23995-8 and 2014/05679-4) for financial support.

References

- [1] A. Feiz, A. Bazgir, Gold nanoparticles supported on mercaptoethanol directly bonded to MCM-41: an efficient catalyst for the synthesis of propargylamines, *Catal. Commun.* 73 (2016) 88–92, <http://dx.doi.org/10.1016/j.catcom.2015.09.028>.
- [2] C.C. Torres, J.B. Alderete, G. Pecchi, C.H. Campos, P. Reyes, B. Pawelec, E.G. Vaschetto, G.A. Eimer, Heterogeneous hydrogenation of nitroaromatic compounds on gold catalysts: influence of titanium substitution in MCM-41 mesoporous supports, *Appl. Catal. A Gen.* 517 (2016) 110–119, <http://dx.doi.org/10.1016/j.apcata.2016.02.013>.
- [3] D.O. Santos, M. de Lourdes Nascimento Santos, J.A.S. Costa, R.A. de Jesus, S. Navickiene, E.M. Sussuchi, M.E. de Mesquita, Investigating the potential of functionalized MCM-41 on adsorption of remazol red dye, *Environ. Sci. Pollut. Res.* 20 (2013) 5028–5035, <http://dx.doi.org/10.1007/s11356-012-1346-6>.
- [4] J.A.S. Costa, A.C.F.S. Garcia, D.O. Santos, V.H.V. Sarmento, A.L.M. Porto, M.E. De Mesquita, L.P.C. Romão, A new functionalized MCM-41 mesoporous material for use in environmental applications, *J. Braz. Chem. Soc.* 25 (2014) 197–207, <http://dx.doi.org/10.5935/0103-5053.20130284>.
- [5] J.A.S. Costa, A.C.F.S. Garcia, D.O. Santos, V.H.V. Sarmento, M.E. de Mesquita, L.P.C. Romão, Applications of inorganic-organic mesoporous materials constructed by self-assembly processes for removal of benzo[k]fluoranthene and benzo[b]fluoranthene, *J. Sol-Gel Sci. Technol.* 75 (2015) 495–507, <http://dx.doi.org/10.1007/s10971-015-3720-6>.
- [6] M.K. Selim, S. Komarneni, M.R. Abu Khadra, Phosphate removal from solution by composite of MCM-41 silica with rice husk: Kinetic and equilibrium studies, *Microporous Mesoporous Mater.* 224 (2016) 51–57, <http://dx.doi.org/10.1016/j.micromeso.2015.11.011>.
- [7] J.A.S. Costa, R.A. de Jesus, C.M.P. da Silva, L.P.C. Romão, Efficient Adsorption of a mixture of polycyclic aromatic hydrocarbons (PAHs) by Si-MCM-41 mesoporous molecular sieve, *Powder Technol.* 308 (2017) 434–441, <http://dx.doi.org/10.1016/j.powtec.2016.12.035>.
- [8] E. Vyskocilová, I. Luštická, I. Paterová, L. MacHová, L. Cervený, Modified MCM-41 as a drug delivery system for acetylsalicylic acid, *Solid State Sci.* 38 (2014) 85–89, <http://dx.doi.org/10.1021/la0267084>.
- [9] B. Yuliarto, I. Honma, Y. Katsumura, H. Zhou, Preparation of room temperature NO₂ gas sensors based on W- and V-modified mesoporous MCM-41 thin films employing surface photovoltage technique, *Sens. Actuators B Chem.* 114 (2006) 109–119, <http://dx.doi.org/10.1016/j.snb.2005.04.016>.
- [10] L. Guangying, F. Jun, A series of phosphorescent Cu(I) complexes: synthesis, photophysical feature and optical oxygen sensing performance in MCM-41 silica matrix,

- Sens. Actuators B Chem. 233 (2016) 347–354, <http://dx.doi.org/10.1016/j.snb.2016.04.078>.
- [11] D. Wang, B. Li, L. Zhang, J. Ying, X. Wu, Preparation, characterization, and luminescence properties of novel hybrid material containing europium(III) complex covalently bonded to MCM-41, *J. Lumin.* 130 (2010) 598–602, <http://dx.doi.org/10.1016/j.jlumin.2009.11.002>.
- [12] Z.A. Alatham, A review: fundamental aspects of silicate mesoporous materials, *Materials* 5 (2012) 2874–2902, <http://dx.doi.org/10.3390/ma5122874>.
- [13] C.T. Kresge, M.E. Leonowicz, W.J. Roth, J.C. Vartuli, J.S. Beck, Ordered mesoporous molecular sieves synthesized by a liquid-crystal template mechanism, *Nature* 355 (1992) 717–719.
- [14] Y.J. Li, B. Yan, L. Wang, Rare earth (Eu^{3+} , Tb^{3+}) mesoporous hybrids with calix[4] arene derivative covalently linking MCM-41: physical characterization and photoluminescence property, *J. Solid State Chem.* 184 (2011) 2571–2579, <http://dx.doi.org/10.1016/j.jssc.2011.07.040>.
- [15] Y.J. Gu, B. Yan, Europium (III) complex functionalized Si-MCM-41 hybrid materials with visible-light-excited luminescence, *Inorg. Chim. Acta.* 408 (2013) 96–102, <http://dx.doi.org/10.1016/j.ica.2013.09.008>.
- [16] Y. Li, B. Yan, Lanthanide (Tb^{3+} , Eu^{3+}) functionalized MCM-41 through modified meta-aminobenzoic acid linkage: covalently bonding assembly, physical characterization and photoluminescence, *Microporous Mesoporous Mater.* 128 (2010) 62–70, <http://dx.doi.org/10.1016/j.micromeso.2009.08.005>.
- [17] A. Fernandes, J. Dexpert-Ghys, A. Gleizes, A. Galarneau, D. Brunel, Grafting luminescent metal-organic species into mesoporous MCM-41 silica from europium(III) tetramethylheptanedionate, $\text{Eu}(\text{thd})_3$, *Microporous Mesoporous Mater.* 83 (2005) 35–46, <http://dx.doi.org/10.1016/j.micromeso.2004.12.026>.
- [18] W. Yin, M. Zhang, Characterization of Nanosized Tb-MCM-41 Synthesized by the Sol-gel-assisted Self-assembly Method, 360, 2003, pp. 231–235.
- [19] B. Yan, Q.P. Li, Photofunctional hybrids of lanthanide (Eu^{3+} , Tb^{3+})/beta-diketone functionalized MCM-41/SBA-15 mesoporous host prepared with 1,4,7,10-tetraazacyclododecane modified siloxane as covalent linkage, *Microporous Mesoporous Mater.* 196 (2014) 284–291, <http://dx.doi.org/10.1016/j.micromeso.2014.05.033>.
- [20] B. Yan, B. Zhou, Two photoactive lanthanide (Eu^{3+} , Tb^{3+}) hybrid materials of modified β -diketone bridge directly covalently bonded mesoporous host (MCM-41), *J. Photochem. Photobiol. A Chem.* 195 (2008) 314–322, <http://dx.doi.org/10.1016/j.jphotochem.2007.10.019>.
- [21] Y. Li, B. Yan, Hybrid materials of MCM-41 functionalized by lanthanide (Tb^{3+} , Eu^{3+}) complexes of modified meta-methylbenzoic acid: covalently bonded assembly and photoluminescence, *J. Solid State Chem.* 181 (2008) 1032–1039, <http://dx.doi.org/10.1016/j.jssc.2008.02.001>.
- [22] X.M. Zang, L.F. Shen, E.Y.B. Pun, J. Guo, H. Lin, Photon quantification of electrospun europium-complexes/PMMA submicron fibers, *J. Alloys Compd.* 709 (2017) 620–626, <http://dx.doi.org/10.1016/j.jallcom.2017.03.178>.
- [23] H. Yu, L. Xia, X.T. Dong, X. Le Zhao, Preparation and luminescent characteristics of $\text{Eu}_2\text{O}_3\text{-ZnO}/(\text{SBA-15})$ composite materials, *J. Lumin.* 158 (2015) 19–26, <http://dx.doi.org/10.1016/j.jlumin.2014.09.022>.
- [24] Y. Wang, H. Li, L. Gu, Q. Gan, Y. Li, G. Calzaferri, Thermally stable luminescent lanthanide complexes in zeolite L, *Microporous Mesoporous Mater.* 121 (2009) 1–6, <http://dx.doi.org/10.1016/j.micromeso.2008.12.028>.
- [25] Q.G. Meng, P. Boutinaud, A.C. Franville, H.J. Zhang, R. Mahiou, Preparation and characterization of luminescent cubic MCM-48 impregnated with an Eu^{3+} β -diketonate complex, *Microporous Mesoporous Mater.* 65 (2003) 127–136, <http://dx.doi.org/10.1016/j.micromeso.2003.07.002>.
- [26] Y. Liu, Z. wei Li, N. Bao, H. Yu, Y. ming Lin, X. ting Dong, H. bo Zhang, L. Xia, D. wei Feng, Y. Juan Yu, Preparation and luminescent properties of (Tb^{3+} - Yb^{3+}) SSA/(SBA-15) composite materials, *J. Lumin.* 180 (2016) 38–45, <http://dx.doi.org/10.1016/j.jlumin.2016.08.002>.
- [27] M. Guan, L. Gao, S. Wang, C. Huang, K. Wang, Syntheses and electroluminescent properties of two europium ternary complexes $\text{Eu}(\text{DBM})_3(\text{PBO})$ and $\text{Eu}(\text{DBM})_3(\text{PBT})$, *J. Lumin.* 127 (2007) 489–493, <http://dx.doi.org/10.1016/j.jlumin.2007.02.042>.
- [28] J.M.F.B. Aquino, A.S. Araujo, D.M.A. Melo, J.E.C. Silva, M.J.B. Souza, A.O.S. Silva, Synthesis, characterization, and luminescent properties of MCM-41 and AlMCM-41 mesoporous materials containing Eu(III) ions, *J. Alloy. Compd.* 374 (2004) 101–104, <http://dx.doi.org/10.1016/j.jallcom.2003.11.075>.
- [29] A.L. Ramirez, K.E. Knope, T.T. Kelley, N.E. Greig, J.D. Einkauf, D.T. De Lill, Inorganica Chimica Acta Structure and luminescence of a 2-dimensional 2, 3-pyridinedicarboxylate coordination polymer constructed from lanthanide (III) dimers, *Inorg. Chim. Acta.* 392 (2012) 46–51, <http://dx.doi.org/10.1016/j.ica.2012.05.039>.
- [30] R.A. de Jesus, L.L. da Luz, D.O. Santos, J.A.S. Costa, S. Navickiene, C.C. Gatto, S.A. Júnior, M.E. de Mesquita, Dual emission tunable in the near-infrared (NIR) and visible (VIS) spectral range by mix-LnMOF, *Dalton Trans.* 44 (2015) 17318–17325, <http://dx.doi.org/10.1039/C5DT01920F>.
- [31] D.L. Pavia, G.M. Lampman, G.S. Kriz, *Introduction to Spectroscopy*, 3rd, Thomson Learning, Inc, Washington D. C, 2001 (680 p.).
- [32] R.M. Braga, J.M.F. Barros, D.M.A. Melo, M.A.F. Melo, F. De, M. Aquino, J.C. Julio, R.C. Santiago, Kinetic study of template removal of MCM-41 derived from rice husk ash, *J. Therm. Anal. Calorim.* 111 (2013) 1013–1018, <http://dx.doi.org/10.1007/s10973-012-2516-y>.
- [33] S. Zheng, L. Gao, J. Guo, Synthesis and characterization of copper(II)-phenanthroline complex grafted organic groups modified MCM-41, *Mater. Chem. Phys.* 71 (2001) 174–178, [http://dx.doi.org/10.1016/S0254-0584\(01\)00276-0](http://dx.doi.org/10.1016/S0254-0584(01)00276-0).
- [34] M.O. Rodrigues, A.M. Brito-silva, S. Alves, C.A. De Simone, A.A.S. Araújo, P.H.V. De Carvalho, S.C.G. Santos, K.A.S. Aragão, R.O. Freire, E. Mesquita, Structural and Spectroscopic Studies of The 2d Coordination Polymers, $\infty[\text{Tb}(\text{DPA})(\text{HDPAA})]$ and $\infty[\text{Gd}(\text{DPA})(\text{HDPAA})]$, 32, 2009, pp. 286–291.
- [35] A.S. Barreto, R.L. Da Silva, S.C.G. Dos Santos Silva, M.O. Rodrigues, C.A. De Simone, G.F. De Sá, S.A. Júnior, S. Navickiene, M.E. De Mesquita, Potential of a metal-organic framework as a new material for solid-phase extraction of pesticides from lettuce (*Lactuca sativa*), with analysis by gas chromatography-mass spectrometry, *J. Sep. Sci.* 33 (2010) 3811–3816, <http://dx.doi.org/10.1002/jssc.201000553>.
- [36] F.G. Freitas, V.H.V. Sarmiento, C.V. Santilli, S.H. Pulcinelli, Controlling the growth of zirconia needles precursor from a liquid crystal template, *Colloids Surf. A Physicochem. Eng. Asp.* 353 (2010) 77–82, <http://dx.doi.org/10.1016/j.colsurfa.2009.10.024>.
- [37] R.A.A. Melo, M.V. Giotto, J. Rocha, E.A. Urquieta-González, MCM-41 ordered mesoporous molecular sieves synthesis and characterization, *Mater. Res.* 2 (1999) 173–179, <http://dx.doi.org/10.1590/S1516-1439199900300010>.
- [38] S.A. Mirji, S.B. Halligudi, D.P. Sawant, N.E. Jacob, K.R. Patil, A.B. Gaikwad, S.D. Pradhan, Adsorption of octadecyltrichlorosilane on mesoporous SBA-15, *Appl. Surf. Sci.* 252 (2006) 4097–4103, <http://dx.doi.org/10.1016/j.apsusc.2005.06.009>.
- [39] A. Tang, Y. Deng, J. Jin, H. Yang, $\text{ZnFe}_2\text{O}_4/\text{TiO}_2$ Nanoparticles within mesoporous MCM-41, *Sci. World J.* 2012 (2012) 1–8, <http://dx.doi.org/10.1100/2012/480527>.
- [40] S. Jabariyan, M.A. Zanjanchi, A simple and fast sonication procedure to remove surfactant templates from mesoporous MCM-41, *Ultrason. Sonochem.* 19 (2012) 1087–1093, <http://dx.doi.org/10.1016/j.ulsonch.2012.01.012>.
- [41] C. Peng, H. Zhang, J. Yu, Q. Meng, L. Fu, H. Li, L. Sun, X. Guo, Synthesis, characterization, and luminescence properties of the ternary europium complex covalently bond to mesoporous SBA-15, *J. Phys. Chem. B* 109 (2005) 15278–15287.
- [42] P.M. Jr., J. Zukerman-Schpector, P.C. Isolani, G. Vicentini, L.B. Zinner, Synthesis and Structure of Lanthanide Picrates with Trans -1,3-dithiane-1,3-dioxide, 344, 2002, pp. 141–144.
- [43] X. Guo, L. Fu, H. Zhang, L.D. Carlos, C. Peng, J. Guo, J. Yu, R. Deng, L. Sun, Incorporation of luminescent lanthanide complex inside the channels of organically modified mesoporous silica via template-ion exchange method, *New J. Chem.* 29 (2005) 1351, <http://dx.doi.org/10.1039/b504707b>.
- [44] F.A. Jesus, S.T.S. Santos, J.M.A. Caiu, V.H.V. Sarmiento, Effects of thermal treatment on the structure and luminescent properties of Eu^{3+} doped SiO_2 -PMMA hybrid nanocomposites prepared by a sol-gel process, *J. Lumin.* 170 (2016) 588–593, <http://dx.doi.org/10.1016/j.jlumin.2015.05.030>.
- [45] Y. Luo, B. Chen, W. Wu, X. Yu, Q. Yan, Q. Zhang, Judd-Ofelt treatment on luminescence of europium complexes with β -diketone and bis(β -diketone), *J. Lumin.* 129 (2009) 1309–1313, <http://dx.doi.org/10.1016/j.jlumin.2009.06.016>.
- [46] I.E. Kolesnikov, D.V. Mamonova, E. Lähderanta, A.V. Kurochkin, M.D. Mikhailov, The impact of doping concentration on structure and photoluminescence of $\text{Lu}_2\text{O}_3\text{:Eu}_3+$ nanocrystals, *J. Lumin.* 187 (2017) 26–32, <http://dx.doi.org/10.1016/j.jlumin.2017.03.006>.
- [47] K.P. Mani, G. Vimal, P.R. Biju, C. Joseph, N.V. Unnikrishnan, M.A. Ittyachen, Structural and spectral investigation of terbium molybdate nanophosphor, *Spectrochim. Acta – Part A Mol. Biomol. Spectrosc.* 148 (2015) 412–419, <http://dx.doi.org/10.1016/j.saa.2015.04.016>.
- [48] M. Massey, M.G. Ancona, L.L. Medintz, W.R. Algar, Time-resolved nucleic acid hybridization beacons utilizing unimolecular and toehold-mediated strand displacement designs, *Anal. Chem.* 87 (2015) 11923–11931, <http://dx.doi.org/10.1021/acs.analchem.5b03618>.
- [49] G.S. Kottas, M. Mehlstäubel, R. Fröhlich, L. De Cola, Highly luminescent, neutral, nine-coordinate lanthanide(III) complexes, *Eur. J. Inorg. Chem.* 1 (2007) 3465–3468, <http://dx.doi.org/10.1002/ejic.200700514>.
- [50] D. Wang, C. Zheng, L. Fan, J. Zheng, X. Wei, Preparation and fluorescent properties of europium (III) complexes with β -diketone ligand and 2,2-dipyridine or 1,10-phenanthroline, *Synth. Met.* 162 (2012) 2063–2068, <http://dx.doi.org/10.1016/j.synthmet.2012.10.014>.
- [51] E.E.S. Teotonio, G.M. Fett, H.F. Brito, W.M. Faustino, G.F. de Sá, M.C.F.C. Felinto, R.H.A. Santos, Evaluation of intramolecular energy transfer process in the lanthanide(III) bis- and tris-(TTA) complexes: photoluminescent and triboluminescent behavior, *J. Lumin.* 128 (2008) 190–198, <http://dx.doi.org/10.1016/j.jlumin.2007.07.005>.
- [52] S.M. Bruno, R.A. Sá Ferreira, L.D. Carlos, M. Pillinger, P. Ribeiro-Claro, I.S. Gonçalves, Synthesis, characterisation and luminescence properties of MCM-41 impregnated with an Eu^{3+} β -diketonate complex, *Microporous Mesoporous Mater.* 113 (2008) 453–462, <http://dx.doi.org/10.1016/j.micromeso.2007.12.004>.
- [53] M. Beltaif, M. Dammak, M. Megdiche, K. Guidara, Synthesis, optical spectroscopy and Judd-Ofelt analysis of Eu^{3+} doped $\text{Li}_2\text{BaP}_2\text{O}_7$ phosphors, *J. Lumin.* 177 (2016) 373–379, <http://dx.doi.org/10.1016/j.jlumin.2016.05.016>.
- [54] M. Ferhi, C. Bouzidi, K. Horchani-Naifer, H. Elhouichet, M. Ferid, Judd-Ofelt analysis of spectroscopic properties of Eu^{3+} doped $\text{KLa}(\text{PO}_3)_4$, *J. Lumin.* 157 (2015) 21–27, <http://dx.doi.org/10.1016/j.jlumin.2014.08.017>.
- [55] M.A. Hassairi, A. Garrido Hernández, T. Kallel, M. Dammak, D. Zambon, G. Chadeyron, A. Potdevin, D. Boyer, R. Mahiou, Spectroscopic properties and Judd-Ofelt analysis of Eu^{3+} doped GdPO_4 nanoparticles and nanowires, *J. Lumin.* 170 (2016) 200–206, <http://dx.doi.org/10.1016/j.jlumin.2015.10.054>.
- [56] T. Koubaa, M. Dammak, M.C. Pujol, M. Aguiló, F. Díaz, Optical spectroscopy of Eu^{3+} ions doped in $\text{KLu}(\text{WO}_4)_2$ single crystals, *J. Lumin.* 168 (2015) 7–13, <http://dx.doi.org/10.1016/j.jlumin.2015.07.015>.
- [57] G. Ramakrishna, H. Nagabhushana, B.D. Prasad, Y.S. Vidya, S.C. Sharma, K.S. Anantharaju, S.C. Prashantha, N. Choudhary, Spectroscopic properties of red emitting Eu^{3+} doped Y_2SiO_5 nanophosphors for WLED's on the basis of Judd-Ofelt analysis: calotropis gigantea latex mediated synthesis, *J. Lumin.* 181 (2017) 153–163, <http://dx.doi.org/10.1016/j.jlumin.2016.08.050>.
- [58] L.D. Carlos, R.A.S. Ferreira, V. De Zea Bermudez, S.J.L. Ribeiro, Lanthanide-containing light-emitting organic-inorganic hybrids: a set on the future, *Adv. Mater.* 21 (2009) 509–534, <http://dx.doi.org/10.1002/adma.200801635>.
- [59] H. Liang, F. Xie, Luminescence of a conjugated polymer containing europium (III) chelate, *J. Lumin.* 144 (2013) 230–233, <http://dx.doi.org/10.1016/j.jlumin.2013.08.014>.